


RESEARCH ARTICLE

Design and optimization of a decoupled serial constant force microgripper for force sensitive objects manipulation

Ye Shan¹, Bingxiao Ding^{2,*}, Jianhua Zhong¹ and Yangmin Li^{2,*} 

¹School of Advanced Manufacturing, Fuzhou University, Quanzhou, 362200, China and ²Department of Industrial and Systems Engineering, The Hong Kong Polytechnic University, Hong Kong, 999077, China

*Corresponding authors. E-mails: bingxding@hotmail.com; yangmin.li@polyu.edu.hk

Received: 25 July 2022; **Revised:** 14 January 2023; **Accepted:** 17 February 2023

Keywords: compliant mechanism; constant force gripper; fully decoupled; FEA optimization

Abstract

To address coupling motion issues and realize large constant force range of microgrippers, we present a serial two-degree-of-freedom compliant constant force microgripper (CCFMG) in this paper. To realize a large output displacement in a compact structure, Scott–Russell displacement amplification mechanisms, bridge-type displacement amplification mechanisms, and lever amplification mechanisms are combined to compensate stroke of piezoelectric actuators. In addition, constant force modules are utilized to achieve a constant force output. We investigated CCFMG's performances by means of pseudo-rigid body models and finite element analysis. Simulation results show that the proposed CCFMG has a stroke of 781.34 μm in the X-direction and a stroke of 258.05 μm in the Y-direction, and the decoupling rates in two directions are 1.1% and 0.9%, respectively. The average output constant force of the clamp is 37.49 N. The amplification ratios of the bridge-type amplifier and the Scott–Russell amplifier are 7.02 and 3, respectively. Through finite element analysis-based optimization, the constant force stroke of CCFMG is increased from the initial 1.6 to 3 mm.

1. Introduction

The compliant-based microgrippers have received widely attention from the field of micro surgery, micro assembly, precision measurement, and micro manipulation due to the recent development of micro electro mechanical systems. Compliant microgripper is one of the key tools to manipulate objects in the micro level [1–4]. Because of compliant microgrippers achieving motion, energy, and forces transmission by elastic deformation of flexure hinges, it avoids backlash, friction, with high repeatable motion and vacuum compatibility [5].

In practical application, the force control of clamping arm is still a tough issue. For example, in the biomedical engineering, the applied excessive force would damage the object and insufficient force cannot hold the object [6]. Traditional force regulation is achieved by adopting advanced force and displacement sensors. However, using sensors realize force control usually have tons of disadvantages. One major drawback is that advanced sensor always matches complex feedback algorithms, it definitely increases the complexity of system [7, 8]. In addition, advanced sensors also increase the cost of the system, and harsh working conditions may lead to accuracy degrading and drop off of sensors. As an alternatively choice, constant force mechanisms (CFM) were developed. Unlike the traditional elastic structure, the CFM has quasi-zero stiffness (QZS) characteristics and don't obey Hooke's law. The CFM can be realized by many methods, and the typical method is by combining positive stiffness mechanism (PSM) with negative stiffness mechanism (NSM) to form QZS [9, 10]. Given these characteristics, CFMs contribute significantly in operating fragile and force sensitive objects [11, 12]. More importantly, using of CFMs can avoid feedback control loops and also more suitable for utilizing in harsh environments [13, 14].

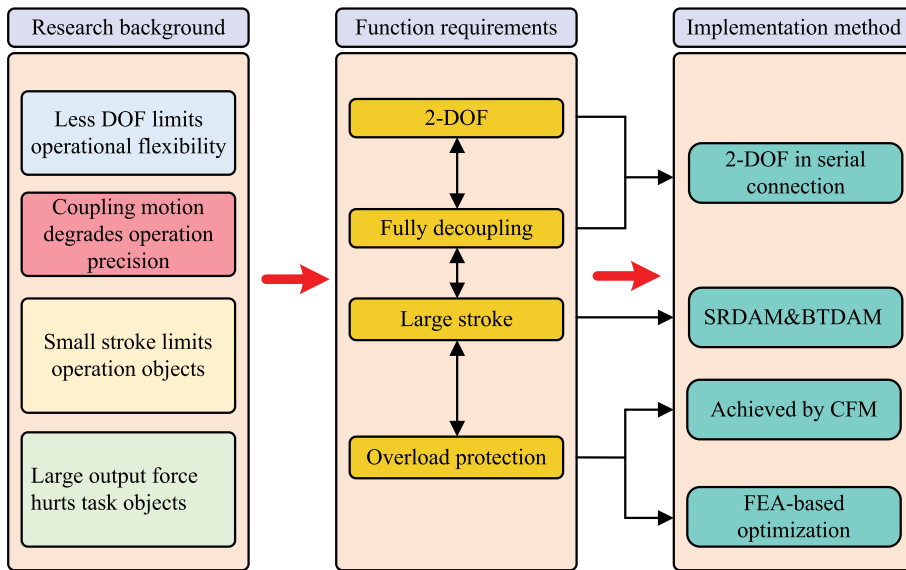


Figure 1. The framework of this study.

In addition, since design parameters of the CFM have a significant impact on its performance, it is necessary to identify optimal parameters combination to get a better performance. The constant force travel range of the CFM determines effective working stroke of the compliant constant force microgripper (CCFMG). To obtain a larger constant force stroke, architectural parameters should be optimized. Referring to previous studies, optimization methods like particle swarm optimization (PSO) and genetic algorithms require complex coding process and also exhibit disadvantages of being easy to fall into local optimal and unable to effectively identify combination optimization parameters [15]. The FEA-based optimization with advantages of easy implementation and recommending the best combination parameters was utilized in this study [16, 17].

Generally, a gripper with 1-DOF is enough to complete gripping operations, and previous works has been devoted by Wang *et al.* [18], Zhao *et al.* [19], Das *et al.* [20]. However, the deficiency is the lack of convenience and flexibility in operation. More DOFs means more flexibility. However, more flexibility means larger space occupation and complex control algorithms. Therefore, 2-DOF microgrippers driven by PEAs which are able to perform dexterous operations have been proposed in recent years [21–24]. However, disadvantages of these microgrippers are obvious. One of the problems is the limited working range due to the limited stroke of PEA. Another problem is the coupling motion in process of clamping objects. Therefore, microgrippers with large operation range, totally decoupling motion and overload protection deserve further study.

Unlike most parallel grippers, a serial 2-DOF CCFMG is proposed in this paper. The horizontal direction motion is mainly responsible for gripping the object, while the vertical direction motion is mainly responsible for approaching the object. Therefore, it can realize totally decoupled motion. In addition, the FEA-based optimization method is utilized to effectively identify optimization parameters. Moreover, to compensate limited stroke of PEA, the SRDAM, lever-type displacement amplification mechanism, and BTDAM are used as hybrid amplification mechanisms to enlarge the clamping range. The framework of this study is depicted in Fig. 1. The rest of this paper is organized as follows. In Section 2, the design and analysis for CCFMG is presented. In Section 3, FEA studies are performed. In Section 4, the parameters optimization are conducted. Finally, some conclusions are drawn in Section 5.

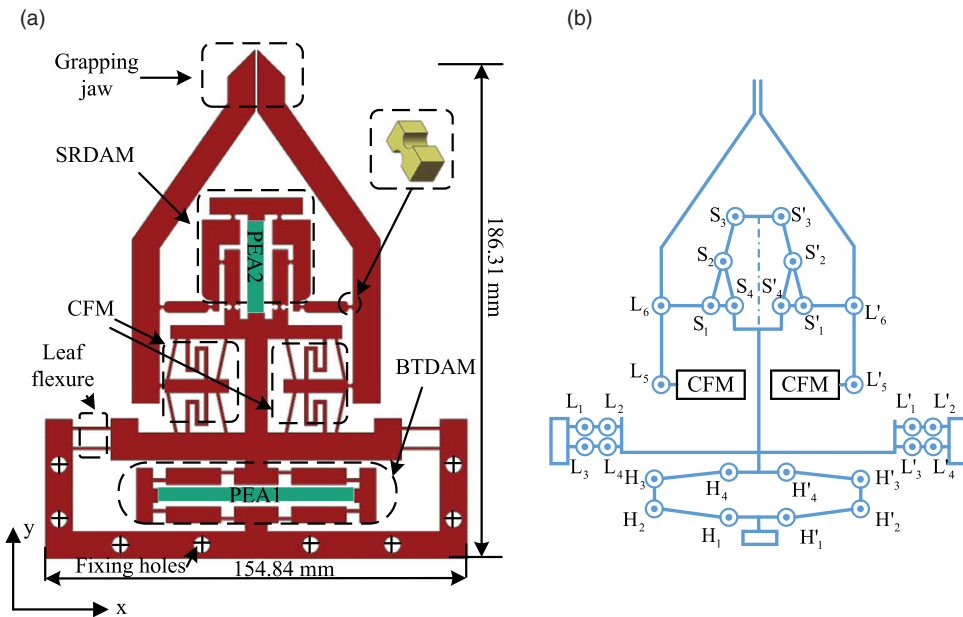


Figure 2. (a) 3D model of CCFMG, (b) the PRBM of CCFMG.

2. Mechanical design

The proposed 2-DOF serial CCFMG is depicted in Fig. 2(a). The whole system consists of two PEAs, a SRDAM, a pair of grasping clamps, two CFM modules, a BTADAM, and a base. The overall dimensions of CCFMG is 186.31 mm × 154.84 mm × 8 mm. For the purpose of obtaining purely parallel movement, the design adopts symmetrical structure. In addition, it also can eliminate temperature effects and provide a more reliable grasping forces. In short, the presented CCFMG has four important features: (1) serial type; (2) 2-DOF with totally decoupling motion; (3) large stroke with hybrid amplification mechanisms in compact size; (4) overload protection using CFM module.

The PRBM diagram of our CCFMG is shown in Fig. 2(b). The motion of CCFMG mainly has two parts. The part of X-direction is consisted of SRDAM and two clamping arm levers. S_3 and S'_3 are the displacement inputs of the SRDAM. The displacement of PEA2 is amplified by SRDAM and provides a double-sided output. The other part mainly consists of one BTADAM and four leaf flexures. The main function of leaf flexures is to connect the gripper and the base. H_2H_3 and $H'_2H'_3$ are the displacement inputs of BTADAM. The displacement of PEA1 is amplified by BTADAM.

2.1. PSM analysis

In this section, force deformation of the Z-beam can be derived referring to previous study [25]. Here, a half of the mechanism is adopted to analysis, concerning its symmetrical structure. The Z-beam consists of three flexible horizontal straight beams and two vertical connecting beams, as is shown in Fig. 3(b). $\theta_1, \theta_2,$ and θ_3 are the deformation angles after the horizontal straight beam subjected to the force, respectively. $l_1, l_2,$ and l_3 are the length of each horizontal straight beam. M_1 is the moment generated at the fixed end of the Z-beam. t and b denote the thickness and width of the Z-beam, respectively. F_p is the reaction force generated along the vertical direction.

The reaction force F_p of the Z-beam can be expressed as

$$F_p = \sum_{i=1}^m F_{p\theta_i} \tag{1}$$

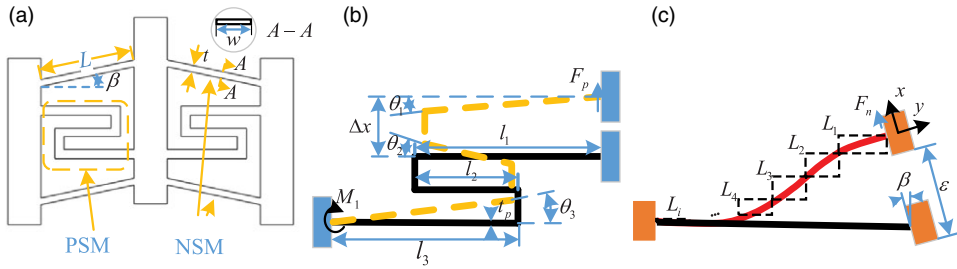


Figure 3. (a) Parameters of CFM, (b) modeling of Z-beam, (c) modeling of bi-stable beam.

where $F_{p\theta_i}$ is the reaction force of a single horizontal straight beam of Z-beam, it can be generated as

$$F_{p\theta_i} = \frac{2EI\theta_i}{l_i^2} \tag{2}$$

where E denotes the Young’s modulus of material, and I is the second moment of area. According to the geometric relationship of the Z-beam, the following equations are derived as

$$\begin{cases} l_1(1 - \cos \theta_1) - l_2(1 - \cos \theta_2) + l_3(1 - \cos \theta_3) = 0 \\ l_1 \sin \theta_1 + l_2 \sin \theta_2 + l_3 \sin \theta_3 = \Delta x \\ \theta_1 = \theta_3 \end{cases} \tag{3}$$

2.2. NSM analysis

A half of the NSM and its architectural parameters are shown in Fig. 3(c). L , t , and ω are the length, thickness, and out-of-plane width of the bi-stable beam, respectively. ϵ is the output displacement of the bi-stable beam by applying force F_n , and β is the angle between the fixed guide beam and the horizontal direction.

The force–displacement expression can be obtained as

$$F_n = ES \frac{\epsilon}{L} \left(\frac{\epsilon}{L} - \sin \theta \right) \left(\frac{\epsilon}{L} - 2 \sin \theta \right) \tag{4}$$

where $S = bt$ is the cross-sectional area of the beam. When θ equals zero, according to Eqs. (2) and (4), the force–displacement relationship of CFM can be obtained

$$\begin{cases} F = \sum_{i=1}^m F_{p\theta_i} + ES \frac{\epsilon}{L} \left(\frac{\epsilon}{L} - \sin \theta \right) \left(\frac{\epsilon}{L} - 2 \sin \theta \right) \\ F = F_n + F_p \end{cases} \tag{5}$$

2.3. Clamping process analysis

The clamping process of proposed CFFMG with overload protection is shown in Fig. 4. During operation of gripping brittle and fragile objects, the BTMAM amplifies PEA1’s displacement in Y direction to approach the object, as shown in Fig. 4(b). When position of jaws is ready, the SRDAM amplifies PEA2’s displacement in X direction to clamp the object, as shown in Fig. 4(b). The large clamping force on the object will trigger the CFM module through the leverage, as shown in Fig. 4(c). Thus, the overload protection is realized. The FEA results comparison is shown in Fig. 4(d), it can be concluded that clamping force F_c applied on the object is 20.8 N, which is much smaller than the initial constant force F 60.25 N.

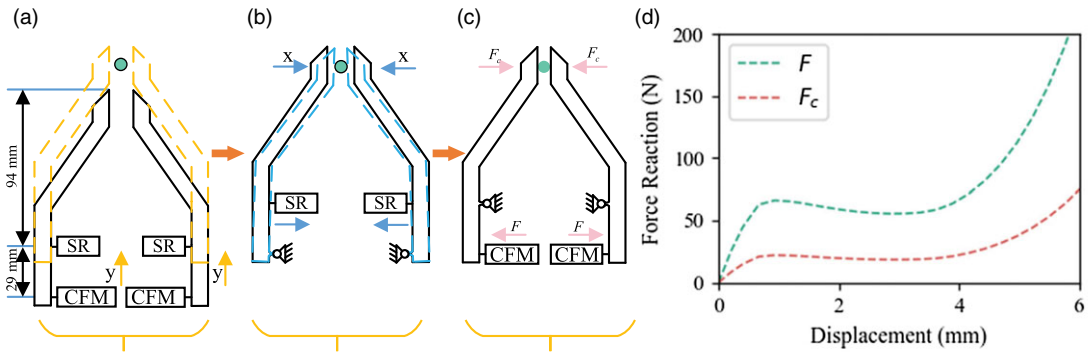


Figure 4. (a) To approach the object, (b) to clamp the object, (c) trigger CFM module to realize overload protection, (d) output constant force comparison before and after triggering CFM module.

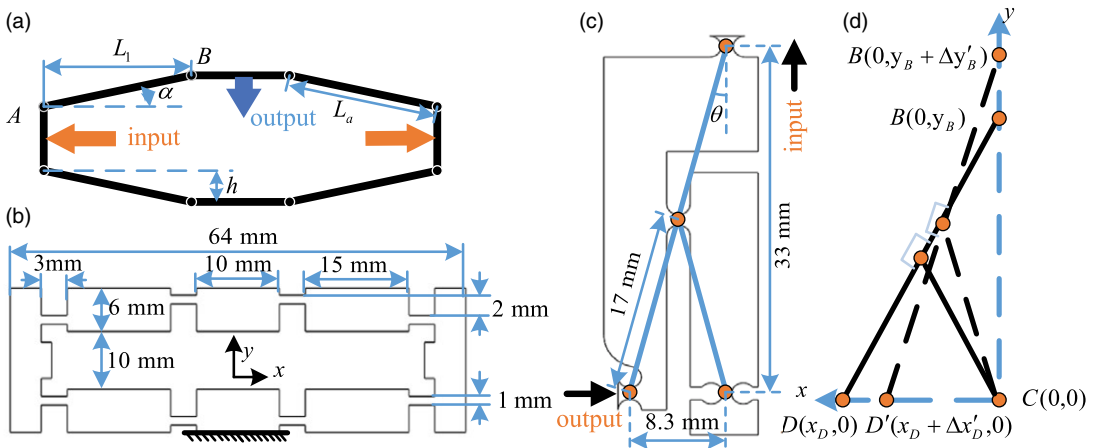


Figure 5. (a) Schematic model of BTMAM, (b) structural dimensions of BTMAM, (c) structural dimensions of SRDAM, (d) schematic model of SRDAM.

2.4. BTMAM analysis

Compared with other displacement amplification mechanisms, the BTMAM takes benefits of large amplification ratio and compactness structure [26]. Therefore, the BTMAM is utilized as the displacement amplifying mechanism in CCFMG.

The PRBM with ideal hinges of BTMAM is shown in Fig. 5(a). The structural parameters of the BTMAM are shown in Fig. 5(b). Due to the bisymmetric structure, only a quarter of the analytical mechanism is analyzed [27, 28].

$$R_{amp,deal} = \frac{h \left[\ln \left(\frac{h}{\sqrt{h^2 + L_1^2}} \right) - \ln \left(\sin \left(\arctan \left(\frac{h}{L_1} \right) - \frac{\Delta x}{h} \right) \right) \right]}{\Delta x} \tag{6}$$

where Δx denotes the input displacement, h is the distance in the vertical direction between the two flexible hinges, and L_1 is the horizontal distance between points A and B . From the data in Fig. 4(b) combined with Eq. (6), it is obtained that $R_{amp,deal} = 6.22$.

Table I. ABS material properties

Property	Young's modulus	Poisson's ratio	Density
Value	2.2 Gpa	0.349	1024 kg/m ³

2.5. SRDAM analysis

The SRDAM can be regarded as an expansion of the slider-crank mechanism. The displacement amplification effect of the SRDAM guarantees the parallel motion of the clamp by producing a wide range of precise linear motion at the output point [29]. The schematic diagram of the circular flexible hinge-based SRDAM is shown in Fig. 5(c). *B* is the displacement input point of the vvPEA, *C* is a fixed hinge, and *D* is the displacement output point of the SRDAM [30]. Let $L_{AC} = L_{AB} = L_{AD} = l$ and $\angle DBC = \theta$. According to the trigonometric relationship, the coordinates of the *D* can be derived

$$\begin{cases} x_D^2 + y_B^2 = 4l^2 \\ y_D = 0 \end{cases} \quad (7)$$

when moving Δy_B along the Y-axis at input point *B*, there will be a corresponding distance Δx_D at output point *D*, i.e.

$$x_D^2 + y_B^2 = (x_D + \Delta x_D)^2 + (y_B + \Delta y_B)^2 \quad (8)$$

Solving Eq. (8), the relationship between Δy_B and Δx_D can be obtained

$$\Delta x_D = -x_D + \sqrt{x_D^2 - 2y_B \Delta y_B - \Delta y_B^2} \quad (9)$$

As $\Delta y_B \rightarrow 0$, then the displacement amplification ratio η_1 can be denoted as

$$\eta_1 = \frac{\Delta x_D}{\Delta y_B} \approx \frac{dx_D}{dy_B} = -\frac{y_B}{\sqrt{4l^2 - y_B^2}} = -\frac{y_B}{x_D} = -\cot \theta \quad (10)$$

From Eq. (10), it can be derived that the η_1 is 3.98. The negative sign indicates that Δy_B and Δx_D are approximately inversely proportional.

3. FEA simulation

To validate the analysis model developed in the previous section, FEA were performed using the ANSYS Workbench to test the performance of the structure. The structure is made of ABS material, which is widely used in 3D printing. The specific material properties are shown in Table I.

3.1. FEA of BTADM

The BTADM is mainly utilized to amplify the output displacement of the PEA1. The enlarged view in Fig. 6 shows two different BTADMs with the same thickness and length of the flexible hinge. Fig. 6(a) and (b) shows the different displacement amplifications, maximum stresses, and corresponding natural frequencies obtained for the BTADM with circular and leaf-shaped flexible hinges, respectively, with the same input displacement. The leaf-shaped flexible hinge has a greater range of rotation than the circular flexible hinge. Thus, the leaf-shaped BTADM typically has a large output displacement, as displayed in Fig. 5(b). From Eq. (6), the theoretical amplification ratio of the BTADM of structural analysis can be derived. The simulation of the BTADM is shown in Fig. 6(b) with the input displacement of 45 μm . The maximum deformation in the output direction is 315.88 μm . Therefore, the displacement amplification R_{sb} of BTADM can be obtained: $R_{sb} = \Delta y / \Delta x = 315.88 / 45 = 7.02$.

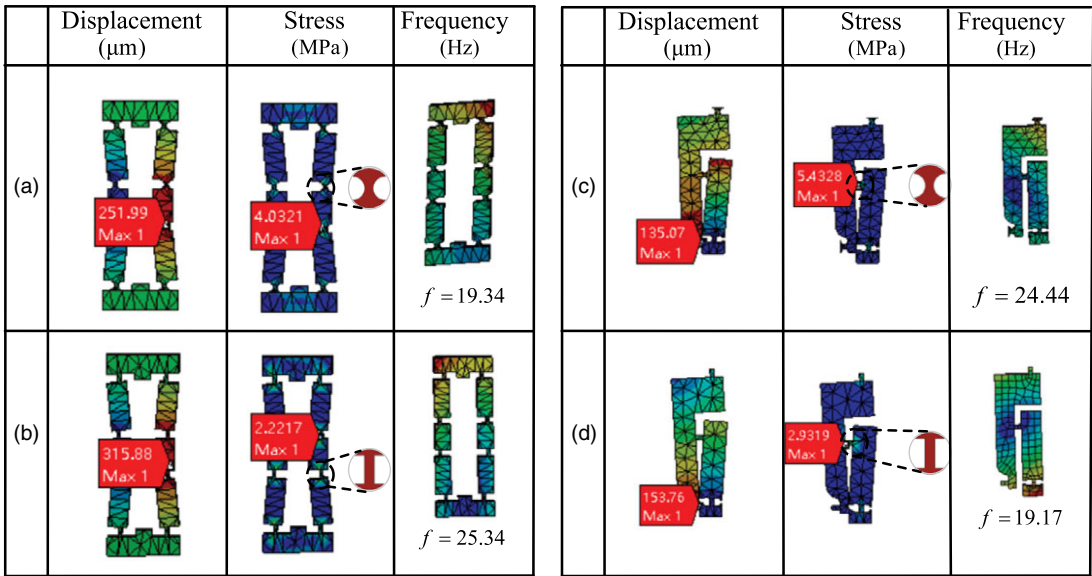


Figure 6. (a) The BT DAM with circular-shaped hinges, (b) the SR DAM with leaf-shaped hinges, (c) the SR DAM with circular-shaped hinges, (d) the SR DAM with leaf-shaped hinges.

3.2. FEA of SR DAM

The SR DAM has two functions, one is to control the motion of the clamping arm through displacement amplification and realize the clamping and releasing of the object. Another role is to act as a pivot point for leverage, a clamp that achieves constant force through leverage. The enlarged view in Fig. 6 shows two different SR DAMs with the same thickness and length of the flexible hinge. Fig. 6(c) and (d) shows the different displacement amplifications, maximum stresses, and corresponding natural frequencies obtained for the SR DAM with circular and leaf-shaped flexible hinges, respectively. Leaf-shaped flexible hinges have a greater range of rotation than right circular flexible hinges. However, the leaf-shaped SR DAM has a lower natural frequency, which reduces the stability and bandwidth during operation and can result in a more pronounced hysteresis of the microgripper, increasing the control difficulty. Therefore, the circular-shaped flexible hinge is selected as the connecting hinge of the SR DAM. The amplification ratio of theoretical amplification can be obtained by Eq. (10). The simulation analysis of the SR DAM is shown in Fig. 6(c), the input displacement is 45 μm, and the maximum displacement at the output side can be seen in Fig. 6(c). Therefore, the displacement amplification R_{ss} of SR DAM can be obtained: $R_{ss} = \Delta y / \Delta x = 135.07 / 45 = 3$.

3.3. Output displacement of the CCFMG clamps

Output displacement of the CCFMG clamp is simulated by ANSYS Workbench. Because the maximum stroke of the selected PEA is 45 μm, the maximum input and output displacements of PEA1 and PEA2 are 45 μm. The PEA2 applies 45 μm stroke at the displacement input of SR DAM, the displacement of a single clamp of the CCFMG in the X-direction after amplification can be obtained, as shown in Fig. 7(a). From the simulation analysis results of FEA, the maximum displacement of a single clamp is 390.67 μm, then the total displacement distance of the two clamps is 781.34 μm. The total displacement amplification ratio in the X-direction is 17.36. Similarly, PEA1 applies 45 μm stroke at the displacement input of BT DAM, then the stroke of CCFMG in the Y-direction can be obtained as shown in Fig. 7(b). The

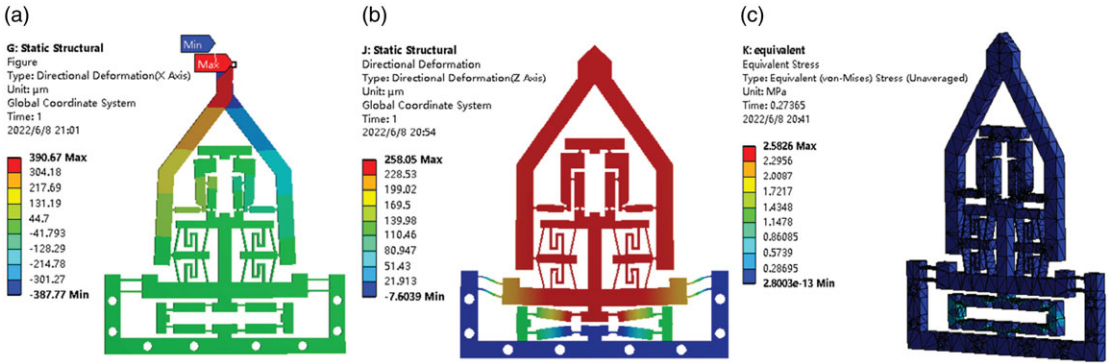


Figure 7. (a) Maximum movement of each jaw in the X-direction for CCFMG, (b) maximum motion of CCFMG in the Y-direction, (c) maximum stress analysis of CCFMG.

total stroke of the clamp of CCFMG in the Y-direction is 258.05 μm , and the displacement amplification ratio is 5.73.

In Table II, R_{SRDAM} and R_{BTDAM} are the displacement amplification rates of SRDAM and BTDAM, respectively. R_{XCFCMG} and R_{YCFCMG} are the total displacement amplification of the CCFMG system in the X and Y directions, respectively. Since there is only one BTDAM displacement amplification mechanism in the Y-direction, the displacement amplification ratio of the CCFMG in the Y-direction is the same as that of the BTDAM. The displacement amplification ratio of SRDAM has the largest error. This is because the increment of displacement in the X-direction is ignored in the model of the theoretical displacement amplification ratio of SRDAM, resulting in insufficient accuracy of the theoretical analysis model.

3.4. Stress analysis

The Fig. 7(c) presents the equivalent stress produced by CCFMG when PEA1 and PEA2 are simultaneously excited for 45 μm . The maximum equivalent stress is 5.601 MPa, which is significantly lower than the tensile strength of the material. The displacements applied to the BTDAM and SRDAM inputs vary simultaneously. The maximum stress of CCFMG is shown in Fig. 7(c). While the PEA1 and PEA2 work together, the equivalent stress will continue to increase as well. Therefore, the safety factor is reduced when the two actuators are operated together and the displacement is large. The safety factor is calculated by $n_{\text{fos}} = \text{yield strength}/\text{tensile strength}$.

In the worst-case scenario, the minimum safety factor is 8.93 when PEA1 and PEA2 output simultaneously 45 μm . If the presented CCFMG is applied to grasp micro-objects, the object size is inversely proportional to the maximum stress of the mechanism, since smaller objects require larger gripping clamp displacements.

3.5. Coupling motion analysis

In this section, decoupling analysis are performed. When applied a input 45 μm displacement on PEA2, the displacement in the X-direction is its working stroke, and displacement along Y-direction is coupling displacement. The corresponding output displacement of individual jaw is shown in Fig. 8(a). It demonstrates that the coupling displacement in the X-direction is 4.21 μm . Similarly, when applied a 45 μm input displacement on the PEA1, the output displacement in Y-direction is shown in Fig. 8(b). The maximum parasitic displacement in X-direction is 2.18 μm . The coupling rates in X-direction and

Table II. Amplification ratio comparisons

Amplification ratio	R_{SRDAM}	R_{BTDAM}	R_{X_CCFMG}	R_{Y_CCFMG}
FEA	3	7.02	8.68	7.02
Theoretical	3.98	6.22	9.24	6.22
Error	24.54%	12.9%	6.06%	12.9%

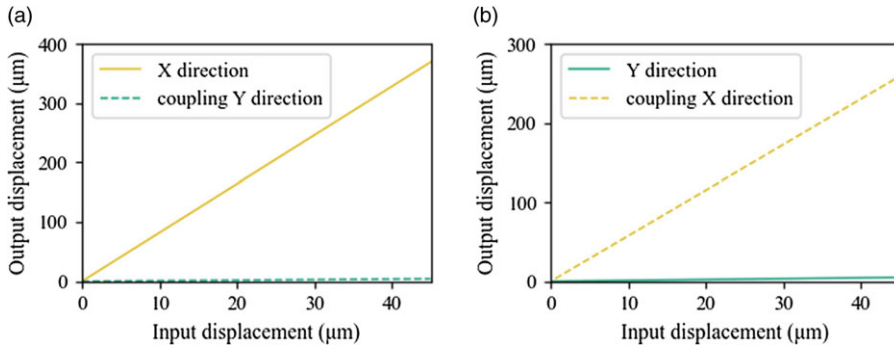


Figure 8. Coupling analysis (a) coupling displacement in Y-direction, (b) coupling displacement in X-direction.

Y-direction are 1.1% and 0.9%, respectively. It can be concluded from FEA results that the proposed CCFMG possesses low coupling ratio.

3.6. Modal analysis

In addition, modal simulations were performed to examine the dynamic performance of the CCFMG structure in terms of resonance modes and frequencies of the CCFMG structure. The simulation results of the six resonance modes are shown in Table III. It can be seen that the first frequency of the CCFMG is 107.16 Hz. The high natural frequency enables the CCFMG device to respond quickly.

From the simulation results, it can be seen that the purpose of the design has been achieved. The CCFMG can provide both a wide range of output and approximate linear motion. The rectilinear movement is useful for grasping various particles in practice.

4. Optimization study

Before conducting parameter optimization, the parameters of CFM must be analyzed to determine the key parameters affecting CFM characteristics. The parameters of the CFM are the length L , thickness t_b , angle β of the bi-stable beam, and the Z-beam length l_1, l_2, l_3 thickness t_z . When analyzing the parameters of the Z-beam, the parameters of the bi-stable beam are kept constant. Let $l_1 = l_3$, when t_z is kept constant, as l_1 changes, l_2 changes accordingly. It is concluded that the independent parameters of the Z-beam are l_2 and t_z . In contrast, when the parameters of the Z-beam are constant, the L changes correspondingly when the β of the bi-stable beam is changed. Therefore, the independent parameters of the bi-stable beam are β and t_b . To sum up, the main structural parameters affecting the CFM are t_b, β, l_2, t_z . Before parameter optimization, the FEA can be used to analyze the influence of four main structural parameters on the CFM characteristics.

When a parameter is analyzed, the other parameters should remain unchanged.

Table III. The first-six resonant frequencies

Mode	1	2	3	4	5	6
Frequency (Hz)	107.16	200.26	225.10	295.42	362.40	574.96

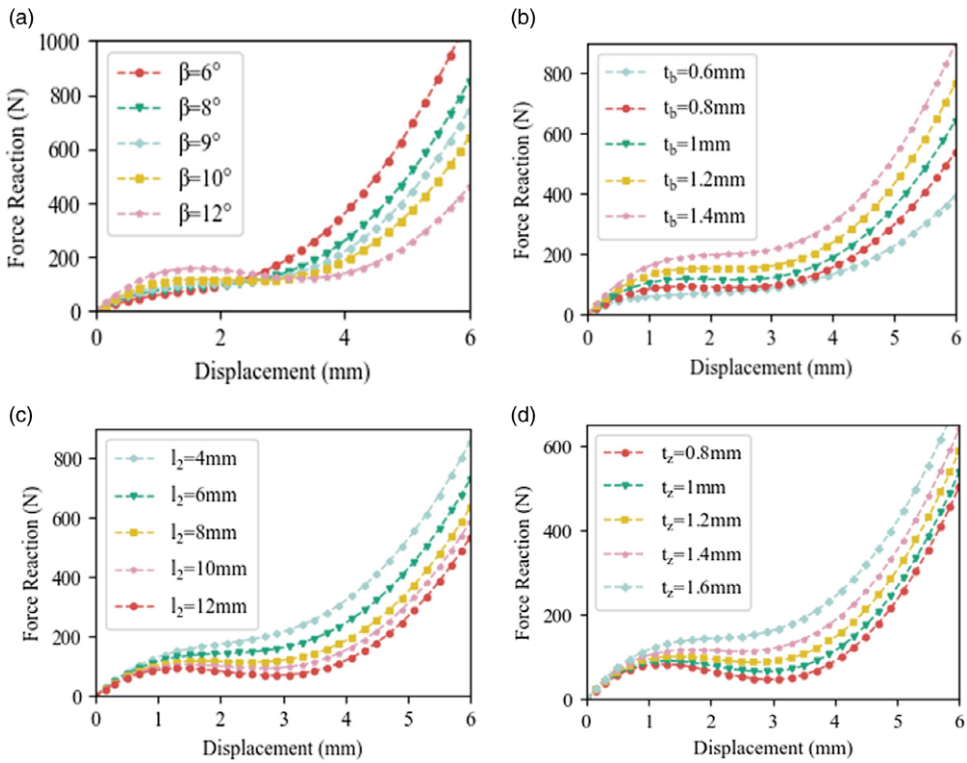


Figure 9. The influence of β , t_b , l_2 , t_z on the constant force properties of the CFM.

Referring to the Fig. 9(a), with increasing the angle of β from 6° to 12° , the characteristics of the bi-stable state become more and more obvious, and subsequently, the magnitude and stroke of the CFM will also increase correspondingly.

In Fig. 9(b), the thickness t_b is increased from 0.6 mm to 1.4 mm with a spacing of 0.2 mm. It can be discovered that t_b has the most significant effect on the characteristics of CFM compared to the other three parameters. With increasing of t_b , the magnitude and stroke of the CFM will also increase.

The effect of thickness t_z on the CFM properties can be studied in Fig. 9(c). The thickness t_z is increased from 0.8 mm to 1.6 mm with 0.2 mm space. Referring to the Fig. 9(c), stroke and force magnitude of the CFM increased correspondingly with increased t_z .

Figure 9(d) shows the effect of changed the l_2 on the characteristics of the CFM. The length l_2 increased from 4 mm to 12 mm, with 2 mm interval. It can be learned that with increased of the length l_2 , the constant force stroke and magnitude of the CFM are decreased.

To make the optimization results more accurate, the response surface optimization module in the ANSYS Workbench optimization module was selected to enable real-time transfer and calculation of data with the static structure analysis module. The optimization process is shown in Fig. 10. Before performing the optimization, it is necessary to define the relationship between the parameters of the mechanical structure and the maximum and minimum values of the parameters.

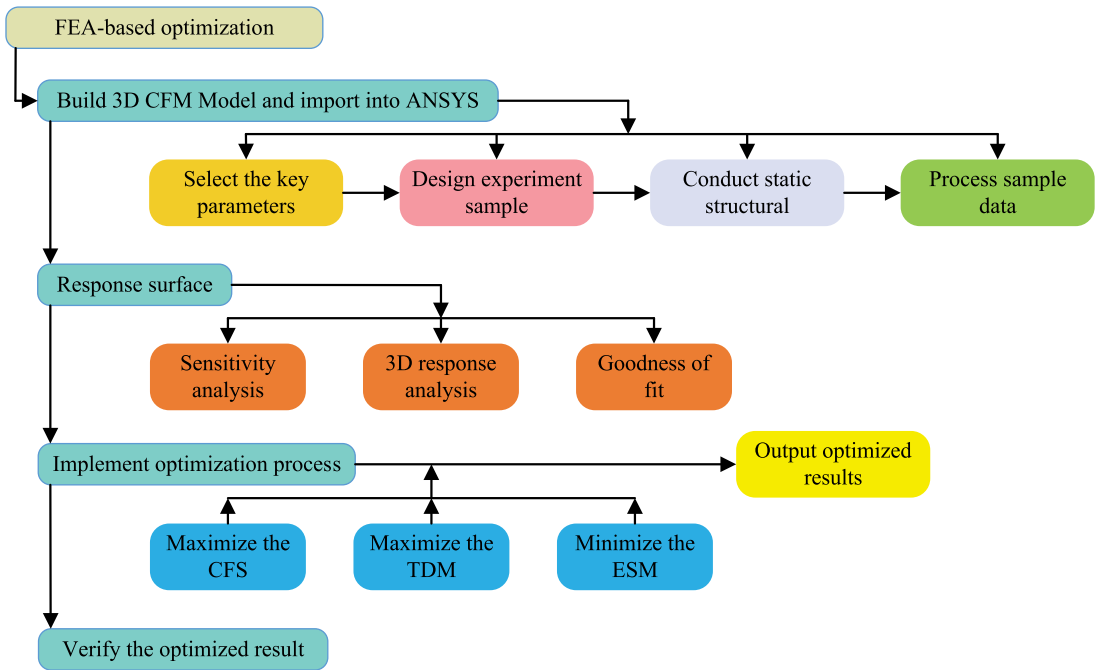


Figure 10. Optimization process.

There are two main parameters to measure the performance of the constant force mechanism, namely, the magnitude and stroke range of the constant force. In this paper, obtaining large constant force stroke is our main purpose.

Since constant-force stroke (CFS) of CFM cannot be measured directly, the CFS is introduced, which defined as the product of CFM stroke and input displacement. Because the input displacement of CFM is constant, the stroke of CFM is proportional to CFS. Furthermore, the total deformation maximum (TDM) and equivalent stress maximum (ESM) were also selected as parameter optimization targets.

In general, the more sample design points, the more accurate the optimization results can be obtained. First, a custom sampling method was used to design the experiment for the four parameters, and the total number of samples was set to 1200. After finite element calculation, the effective samples were 1193. Second, response surface analysis is performed on the effective samples obtained from the calculation, and the fitted relationship between the calculated observations of the target parameters and the response surface predictions can be obtained, as shown in Fig. 11. It can be observed that the observed from the design point is consistent with the predicted from the response surface.

Simultaneously, the trend of the influence of different structural parameters on the optimization objective can be obtained from the response surface analysis. The results of the analysis of the relationship between the specific parameters are presented in Fig. 12.

According to Fig. 12, it can be concluded as follows:

1. In Fig. 12(a) and (b), increasing t_b and β induces an increase in ESM, increasing l_2 causes CFS to decrease. Moreover, the increase of t_z has almost no effect on ESM.
2. In Fig. 12(c) and (d), to increase t_z causes CFS to increase, increasing t_b causes CFS to decrease. Moreover, the increase in β had almost no impact on CFS.

It can be demonstrated that different structural parameters have different degrees of influence on the optimization objectives from response surface analysis. In the meantime, sensitivity analysis between structural parameters and optimization target parameters is also provided in response surface analysis,

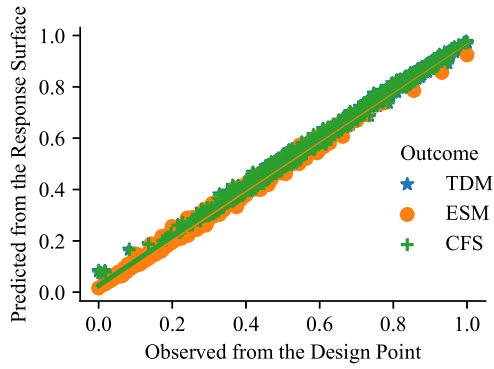


Figure 11. The fitting curves of predicted and observed values.

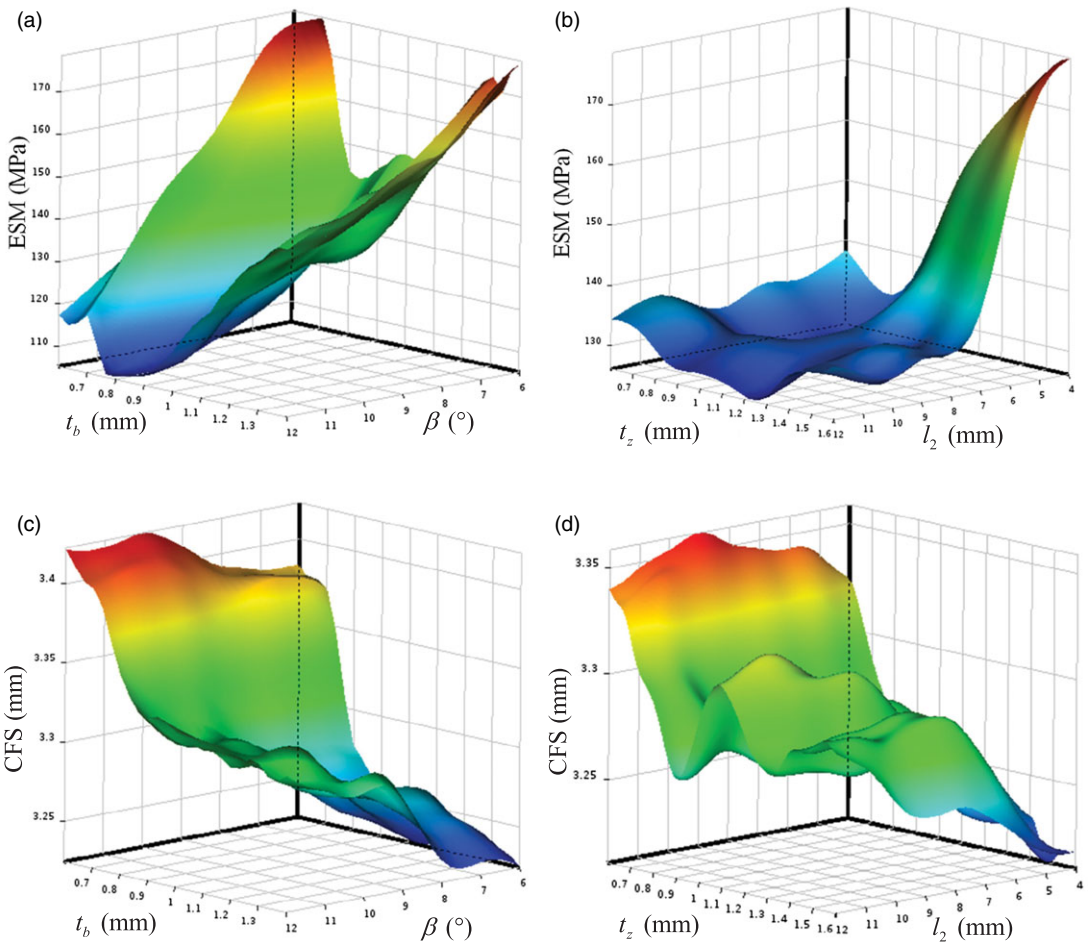


Figure 12. Response surface of CFS and ESM with respect to parameters of β , t_b , l_2 , t_z .

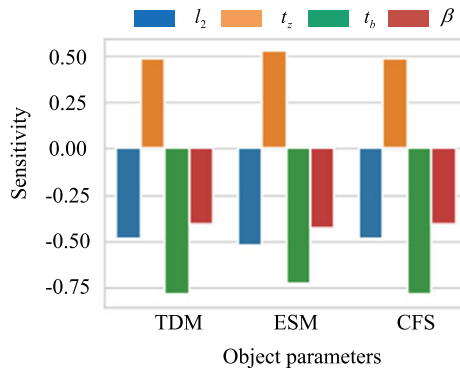


Figure 13. Sensitivity analysis of parameters.

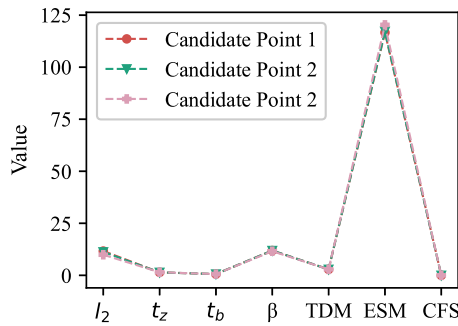


Figure 14. Optimization candidate points.

as shown in Fig. 13. It can be observed that the four structural parameters have positive and negative effects on the target parameters. The effects of a single structural parameter on CFS and TDM are the same, and t_b has the most impact on the two target parameters. The effect of β on the target parameters is minimal.

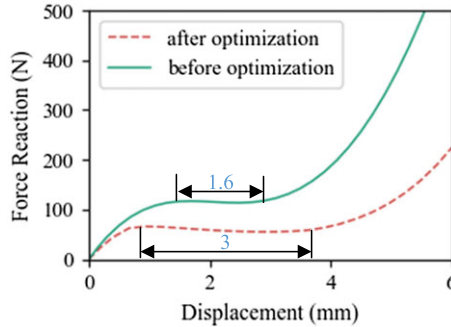
The optimization goals must be set prior to the optimization process. The optimization objectives are to maximize CFS and TDM as well as to minimize ESM. A multiobjective genetic algorithm is available in the module for response surface optimization. This kind of method is suitable to solve multiple inputs and multiple outputs optimization issues, recommending the optimal combinations of structural parameters, obtaining the relationship between the target parameters and optimized parameters. According to the optimization objective, three groups of candidate points for optimal results can be obtained, as shown in Fig. 14.

The optimization system gives three groups of candidate points. First, according to the candidate points, the 3D-model was made up and conducted the static structural in the ANSYS. After comparing the constant force characteristics of the structures constructed from the three groups of sample points, the second group was selected as the final optimal result because it has a longer constant force travel compared to the other two groups. The specific parameters of the second group of optimized values are shown in Table IV.

Constant force curves comparison with optimized parameters and initial parameters are presented in Fig. 15. Referring to the obtained results, the CFS is increased from 1.6 mm to 3 mm after optimization conducted. Although the magnitude of the constant force is smaller, the stroke of the constant force increases more obviously. A larger constant force travel means that the CCFMG is able to grip larger objects, which is more important for CCFMG. The optimized results verified that the multiobjective genetic algorithm is very effective.

Table IV. Obtained optimized values

Parameters	l_2	t_z	β	t_b
Values	11.26 mm	1.4228 mm	0.61815°	11.901 mm

**Figure 15.** Results comparison.

5. Conclusions

A serial decoupled 2-DOF CCFMG is proposed in this paper. Each clamp arm is integrated with a CFM module which formed by NSM and bi-stable beam to achieve a constant clamping force and provide overload protection for fragile objects. Considering PEA's limited stroke, BTMAM and SRMAM were integrated in the design. It can be concluded that stroke of the CCFMG in the gripping direction is 781.34 μm , and the total magnification ratio is 17.36. The stroke in Y-direction is 258.05 μm . The average constant force of the clamp is 37.49 N. The total maximum equivalent stress is 5.601 MPa. Finally, FEA-based optimization was used to identify optimal parameters of CFM for obtaining large stroke. Compared to the initial parameters, the constant force range of the optimized CFM increased from 1.6 mm to 3 mm, an increase of 87.5%.

Author contributions. Ye Shan and Bingxiao Ding conceived and designed this study. Ye Shan conducted data gathering, performed statistical analysis, and wrote the article. Bingxiao Ding, Yangmin Li and Jianhua Zhong revised the manuscript, obtained fund, and supervised the study. All authors have read and agreed to the published version of the manuscript.

Financial support. This work was supported by the Huxiang High-Level Talent Project of Hunan Province (Grant No. 2019RS1066), the State Key Laboratory of Ultra-precision Machining Technology of Hong Kong Polytechnic University (Project No. UAPM).

Conflicts of interest. The authors declare no conflicts of interest exist.

References

- [1] A. M. El-Sayed, A. Abo-Ismael, M. T. El-Melegy, N. A. Hamzaid and N. A. A. Osman, "Development of a micro-gripper using piezoelectric bimorphs," *Sensors* **13**(5), 5826–5840 (2013).
- [2] T. K. Das, B. Shirinzadeh, M. Ghafarian and J. Pinskiar, "A Flexure-Based 2-DOF Microgripper for Handling Micro-Objects," *In: International Conference on Manipulation, Automation and Robotics at Small Scales* (2018) pp. 1–6.
- [3] S. Jun, X. Zhou, D. K. Ramsey and V. N. Krovi, "Smart knee brace design with parallel coupled compliant plate mechanism and pennate elastic band spring," *J. Mech. Robot.* **7**(4), 041024 (2015).
- [4] C. H. Liu, C. H. Chiu, M. C. Hsu and Y. P. Chiang, "Topology and size-shape optimization of an adaptive compliant gripper with high mechanical advantage for grasping irregular objects," *Robotica* **37**(1), 1383–1400 (2019).
- [5] B. X. Ding, Z. X. Yang and Y. M. Li, "Design of flexure-based modular architecture micro-positioning stage," *Microsyst. Technol.* **26**(9), 2893–2901 (2020).
- [6] J. Q. Gan, H. Xu, X. M. Zhang and H. F. Ding, "Design of a compliant adjustable constant-force gripper based on circular beams," *Mech. Mach. Theory* **173**, 104843 (2022).

- [7] M. N. M. Zubir, B. Shirinzadeh and Y. L. Tian, "Development of a novel flexure-based microgripper for high precision micro-object manipulation," *Sens. Actuator A Phys.* **150**(2), 257–266 (2009).
- [8] S. A. Bazaz, F. Khan and R. I. Shakoor, "Design, simulation and testing of electrostatic SOI MUMPs based microgripper integrated with capacitive contact sensor," *Sens. Actuator A Phys.* **167**(1), 44–53 (2011).
- [9] J. Y. Wang and C. C. Lan, "A constant-force compliant gripper for handling objects of various sizes," *J. Mech. Des.* **136**(7), 071008 (2014).
- [10] B. X. Ding, X. Li and Y. M. Li, "Configuration design and experimental verification of a variable constant-force compliant mechanism," *Robotica* **40**(10), 3463–3475 (2022).
- [11] J. Ling, T. T. Ye, Z. Feng, Y. C. Zhu, Y. M. Li and X. H. Xiao, "A survey on synthesis of compliant constant force/torque mechanisms," *Mech. Mach. Theory* **176**, 104970 (2022).
- [12] Y. H. Chen and C. C. Lan, "An adjustable constant-force mechanism for adaptive end-effector operations," *J. Mech. Des.* **134**(3), 031005 (2012).
- [13] H. T. Pham and D. A. Wang, "A constant-force bistable mechanism for force regulation and overload protection," *Mech. Mach. Theory* **46**(7), 899–909 (2011).
- [14] W. Dong, F. X. Chen, Z. J. Du, J. Tang and Z. Dan, "Development of a highly efficient bridge-type mechanism based on negative stiffness," *Smart Mater. Struct.* **26**(9), 095053 (2017).
- [15] R. Y. Jin, P. L. Rocco and Y. H. Ghen, "Cartesian trajectory planning of space robots using a multi-objective optimization," *Aerosp. Sci. Technol.* **108**(106360), 1–11 (2021).
- [16] G. Mohammadali, S. Bijan, A. J. Ammar, K. D. Tilok and P. Joshua, "FEA-based optimization of a complete structure of a monolithic z/tip/tilt micromanipulator," *J. Micro-Bio Robot.* **16**(7), 1–18 (2020).
- [17] B. X. Ding, X. Li and Y. M. Li, "FEA-based optimization and experimental verification of a typical flexure-based constant force module," *Sens. Actuator A Phys.* **332**(1), 113083 (2021).
- [18] D. H. Wang, Q. Yang and H. M. Dong, "A monolithic compliant piezoelectric-driven microgripper: Design, modeling, and testing," *IEEE-ASME Trans. Mechatron.* **18**(1), 138–147 (2013).
- [19] Y. R. Zhao, X. J. Huang, Y. Liu, G. Wang and K. P. Hong, "Design and control of a piezoelectric-driven microgripper perceiving displacement and gripping force," *Micromachines* **11**(2), 121 (2020).
- [20] T. K. Das, B. Shirinzadeh, M. Ghafarian and A. Al-Jodah, "Design, analysis, and experimental investigation of a single-stage and low parasitic motion piezoelectric actuated microgripper," *Smart Mater. Struct.* **29**(4), 045028 (2020).
- [21] S. G. Song, Y. L. Yang, L. Fu, G. P. Li and Y. D. Wei, "Design and analysis of a two-degrees-of-freedom monolithic compliant piezoelectric microgripper," *J. Intell. Mater. Syst. Struct.* **33**(17), 2176–2196 (2022).
- [22] R. D. Souza, K. P. Navin, T. Theodoridis and P. Sharma, "Design, fabrication and testing of a 2 DOF compliant flexural microgripper," *Microsyst. Technol.* **24**(9), 3867–3883 (2018).
- [23] X. Z. Zhang and Q. S. Xu, "Design and analysis of a 2-DOF compliant gripper with constant-force flexure mechanism," *J. Micro-Bio. Robot.* **15**(1), 31–42 (2019).
- [24] W. H. Chen, J. J. Qu, W. J. Chen and J. B. Zhang, "A compliant dual-axis gripper with integrated position and force sensing," *Mechatronics* **47**, 105–115 (2017).
- [25] J. Zhao, J. Y. He, X. P. He and H. X. Wang, "Post-buckling and snap-through behavior of inclined slender beams," *J. Appl. Mech.* **75**(4), 041020 (2008).
- [26] N. Lobontiu and E. Garcia, "Analytical model of displacement amplification and stiffness optimization for a class of flexure-based compliant mechanisms," *Comput. Struct.* **81**(32), 2797–2810 (2003).
- [27] J. H. Pinskiar, B. J. Shirinzadeh, L. Lark, Y. D. Qin and S. Fatikow, "Design, development and analysis of a haptic-enabled modular flexure-based manipulator," *Mechatronics* **40**, 156–166 (2016).
- [28] K. Q. Qi, Y. Xiang, C. Fang, Y. Zhang and C. S. Yu, "Analysis of the displacement amplification ratio of bridge-type mechanism," *Mech. Mach. Theory* **87**, 45–56 (2015).
- [29] Y. L. Tian, B. Shirinzadeh, D. W. Zhang and C. Alici, "Development and dynamic modelling of a flexure-based Scott-Russell mechanism for nano-manipulation," *Mech. Syst. Signal Process.* **23**(3), 957–978 (2009).
- [30] C. M. Chen, Y. C. Hsu and R. F. Fung, "System identification of a Scott-Russell amplifying mechanism with offset driven by a piezoelectric actuator," *Appl. Math. Model.* **36**(6), 2788–2802 (2012).